Available online at www.sciencedirect.com
ScienceDirect
Trans. Nonferrous Met. Soc. China 35(2025) 4050−4064
Transactions of Nonferrous Metals Society of China
www.tnmsc.cn

Achieving high strength of as-extruded Mg−Bi−Ca ternary alloy via rotary swaging and subsequent aging process

Yang CHEN[1], Jun-jie HE[1], Kun YANG[1], Qiu-yan HUANG[2], Hui-jun HAO[1], Yi-lun ZHOU[1], Wei-qi WANG[1], Kai XIONG[1], Yong MAO[1], Qing-hang WANG[3]

1. Materials Genome Institute, School of Materials and Energy, Yunnan University, Kunming 650504, China;
2. Institute of Metal Research, Chinese Academy of Sciences, Shenyang 110016, China;
3. School of Mechanical Engineering, Yangzhou University, Yangzhou 225127, China

Received 15 April 2024; accepted 26 December 2024

Abstract: A Mg−3.2Bi−0.8Ca (BX31, wt.%) ternary alloy with a yield strength of ~358.1 MPa was fabricated by hot extrusion, room-temperature (RT) rotary swaging and subsequent aging treatment. A fine grain structure (~2 μm) and a few secondary phases were observed in the as-extruded alloy, accompanied by a weak non-basal texture. After RT rotary swaging, the average grain size was reduced to ~1 μm via continuous dynamic recrystallization (CDRX). In addition, a large number of residual dislocations piled up within the grain interior, along with the dynamic precipitation of nano-phases. Peak aging occurred rapidly at 448 K for 35 min. After aging, the grain size hardly changed, the density of residual dislocations slightly decreased, and a large number of nano-precipitates were introduced at the dislocation pile-up sites. The grain boundary strengthening, dislocation strengthening and precipitation strengthening co-dominated the strength of the as-aged alloy.

Key words: Mg−Bi−Ca alloy; rotary swaging; aging; continuous dynamic recrystallization; precipitation

1 Introduction

Magnesium (Mg) and its alloys have emerged as highly promising metallic structural materials in the transportation and aerospace sectors, attributed to their low density, high specific strength and stiffness, and excellent damping performance [1−5]. However, the relatively low absolute strengths of Mg alloys, compared with certain steel and aluminum alloys, significantly limit their potential applications. Previous studies have demonstrated that the incorporation of rare earth (RE) elements can effectively enhance the properties of Mg alloys. For example, LI et al [6] reported that adding 0.3 wt.% Ce to pure Mg resulted in a yield strength of 352 MPa for the extruded alloy. Similarly, the elongation at break of the Mg−Zn−Gd alloy, investigated by JIANG et al [7] could be twice that of the AZ31 alloy. Nevertheless, the high cost associated with RE elements renders mass production unfeasible. Therefore, there is an urgent need to develop high-strength Mg alloys devoid of RE elements.

RE-free high-strength Mg alloys can be found in various systems and exhibit mechanical properties comparable to Mg alloys containing RE elements [8]. For instance, a submicron Mg−2Sn−2Ca alloy was obtained through rapid extrusion, where the addition of Ca promoted pyramidal slip activation, resulting in high strength while maintaining excellent elongation (~8%) [9].

Corresponding author: Jun-jie HE, Tel: +86-13340356562, E-mail: 20210015@ynu.edu.cn;
Qing-hang WANG, Tel: +86-18883725047, E-mail: wangqinghang@yzu.edu.cn
https://doi.org/10.1016/S1003-6326(25)66929-9

An as-extruded Mg−1.8Zn−0.1Ca alloy achieved balanced mechanical properties, with a yield strength of 285 MPa and an elongation of 9.1% mainly due to the formation of a typical bimodal structure composed of fine and coarse grains [10]. The microalloying of Mg−1.0Ca−1.0Al−0.2Zn−0.1Mn (XAZM) alloys with various elements results in the formation of dense sub-grains, reduced residual dislocations, fewer coarse particles, and weaker basal textures when leaner alloy additions and higher extrusion temperatures are employed. The XAZM alloy demonstrates exceptional mechanical properties, exhibiting a YS of approximately 425 MPa and an EL of around 11% [11]. These values are comparable to those observed in most rare earth magnesium alloys. In addition to the common Mg−Zn and Mg−Al systems, Mg−Bi-based alloy systems also have the potential for high strength-plasticity synergy.

Mg−Bi-based alloys have attracted considerable attention in recent research as a promising emerging alloy system [12,13] owing to their superior corrosion resistance, thermal stability, and biocompatibility. Bismuth (Bi) is neither essential nor beneficial in mammals and exhibits minimal biological activity. REMENNIK et al [14] developed an innovative class of biocompatible alloys based on the Mg−Bi system, demonstrating a mild foreign body reaction and enhanced bone formation observed around the Mg−Bi−Ca alloy implant. These advanced alloy systems are emerging as viable candidates for biomaterials. Furthermore, the mechanical properties of the Mg−Bi−Ca ternary alloy system show potential to rival those of commercial Mg alloy systems [15]. MENG et al [16] investigated the Mg−Bi−Ca ternary alloy and found that its strength and ductility in the extruded state exceeded those of AZ31.

In a previous study [17], we developed a Ca-containing Mg−3.2Bi−0.8Ca (BX31, wt.%) alloy that demonstrated high strain hardening capacity; however, it exhibited a relatively low tensile yield strength (TYS). For as-extruded BX31 alloy, the high strain-hardening is mainly caused by multiple slip systems and $\{10\bar{1}2\}$ extension twinning during the tensile deformation. The hetero-deformation induced (HDI) stress was found, and its origin was mainly attributed to the distinct Schmid factor (SF) and the low geometrical compatibility factor (m') between adjacent grains. On the other hand, the basal $\langle a \rangle$ screw dislocations in $\{10\bar{1}2\}$ extension twin interiors were observed, which also provided the extra strain hardening capacity.

Over the past decade, severe plastic deformation (SPD) technologies, including equal channel angular pressing (ECAP) and high-pressure torsion (HPT), have been continuously refined to enhance the strength of Mg alloys [18−22]. For instance, ZHANG et al [23] demonstrated that HPT led to significant grain refinement from approximately 250 μm to around 200 nm, accompanied by a hardness increase from approximately HV 60 to about HV 140 in an AZ80 alloy. However, these aforementioned methods remain largely confined to laboratory settings and present challenges for industrial implementation.

Rotary swaging (RS) is regarded as a novel and efficient processing technique for producing high-performance metallic materials such as titanium alloys [24], within the industrial sector. Recently, RS technology has also been utilized by several researchers to refine grain size and enhance the mechanical properties of Mg alloys [25−27]. For example, WAN et al [28] successfully fabricated a nano-crystalline Mg−Gd−Y−Zr alloy via RS process, achieving a yield strength of 650 MPa. HUANG et al [29] reported that by integrating cold RS with aging treatment, the grain size of an extruded WE43 alloy was remarkably refined to approximately 82 nm alongside substantial precipitate formation, resulting in an ultra-high yield strength of ~477 MPa.

In order to further enhance TYS, we attempted to use RS technology. Additionally, it has been observed that the Mg−Bi−Ca system exhibits precipitation during heat treatment [15,16], and numerous high-strength Mg alloys have been successfully fabricated through a combination of SPD and low-temperature aging treatment. LIU et al [30] reported an increase of yield strength by approximately 80 MPa for a Mg−Gd−Y−Zn−Cu−Ni alloy after exposure at 473 K for 66 h. KIM et al [31] proposed a technique involving high-ratio differential speed rolling combined with low-temperature aging which yielded AZ91 alloy sheets exhibiting remarkable yield strength exceeding 400 MPa along with tensile elongations of around 13%.

In this study, we prepared an as-extruded BX31 alloy rod, which was subsequently subjected to RS and aging treatments. This process achieved a TYS of 358.1 MPa and an ultimate tensile strength (UTS) of 375.8 MPa. The microstructures and mechanical properties of the BX31 alloy in different states were comprehensively investigated.

2 Experimental

2.1 Sample preparation

A BX31 alloy ingot with a dimension of *d*85 mm × 200 mm was fabricated by melting high-purity Mg, Mg−10Bi (wt.%) and Mg−25Ca (wt.%) master alloy in a steel crucible under the atmosphere of SF_6 and CO_2 mixed gas (the mixing volume ratio was 1:99). The ingot was homogenized at 773 K for 24 h, and then extruded at 573 K into bar billets of 20 mm in diameter [17] for RS. One up to three passes of rotary swaging were ultimately carried out at room temperature to get diameters of 19.5, 19 and 18.5 mm (corresponding area reductions of 5, 10 and 16%), respectively. The subsequent aging processes were performed at 448 K [28,29] for different time in a vacuum annealing furnace.

2.2 Mechanical properties testing

The Vickers micro-hardness test was performed using an MHV-1000 tester with a load of 19.6 N and a dwell time of 10 s. The mechanical testing machine (ETM-205D) was employed to perform tensile tests at room temperature in a direction parallel to the bar axis and employing an initial strain rate of 1×10^{-3} s^{-1}. The dog-bone-shaped tensile specimens measuring 16 mm × 6 mm × 2 mm in gauge length (along the extrusion direction (ED), width and thickness were fabricated via spark machining. Three tensile specimens were tested to obtain reliable results.

2.3 Microstructural observation

Phase constitution and dislocation density were analyzed by X-ray diffraction (XRD, TTE III) using Cu K_α radiation at a scanning speed of 2 (°)/min. Scanning electron microscopy (SEM, FEOL-JSM7800F) equipped with an Oxford Aztec electron backscatter diffraction (EBSD) probe and transmission electron microscope (TEM, FEI Talos F200X) were employed to observe the microstructures and texture. Samples for EBSD were prepared by mechanical polishing and subsequent electron-polishing (by AC2 at 20 V and 0.05 A for 90 s at −35 ℃), and the step size for EBSD measurement depended on the grain size of the tested microstructure and ranged from 0.1 to 0.15 μm. Commercial HKL Channel 5 software was used to analyze raw EBSD data. The foils for TEM observations were fabricated by mechanical polishing to 60 μm and then punched into disks of 3 mm in diameter. Subsequently, the treated foils were further thinned by ion beam milling.

3 Results

3.1 Microstructures

Figures 1(a−c) show the inverse pole figure (IPF) orientation maps corresponding to longitudinal sections of alloys in the as-extruded, as-swaged, and peak-aged conditions. The white background indicates the zero analytic location based on EBSD analysis. The as-extruded alloy was characterized by a complete dynamic recrystallization (DRX) microstructure with an average grain size of approximately 2.1 μm, accompanied by a weak $\langle 2\bar{1}\bar{1}1\rangle$//ED texture (as illustrated in Figs. 1(a) and (g)). Following RS, the average grain size decreased to approximately 1.0 μm, with a notably sparse occurrence of extension twins at an angle of 86° (designated as T in Fig. 1(b)). Concurrently, the texture transformed from a weak $\langle 2\bar{1}\bar{1}1\rangle$//ED to a pronounced $\langle 10\bar{1}0\rangle$//ED (Fig. 1(g)), and the change in the grains' orientation distribution confirmed that the multiple slip systems were activated during the RS process. Subsequent aging (peak aging time of ~35 min, see Fig. 2) did not alter either the grain size or texture of the peak-aged alloy (Figs. 1(c) and (g)). Compared to the as-extruded BX31 alloy, Vickers micro-hardness increased from 56 to 69, indicating a significant enhancement in the tensile strength of the aged sample. On the other hand, Figs. 1(d−f) display the Kernel average misorientation (KAM) distribution maps along with corresponding average KAM values for the as-extruded, as-swaged, and peak-aged alloys. The as-swaged alloy exhibits an increased average KAM value of ~1.118° compared to ~0.622° for the as-extruded alloy, suggesting substantial

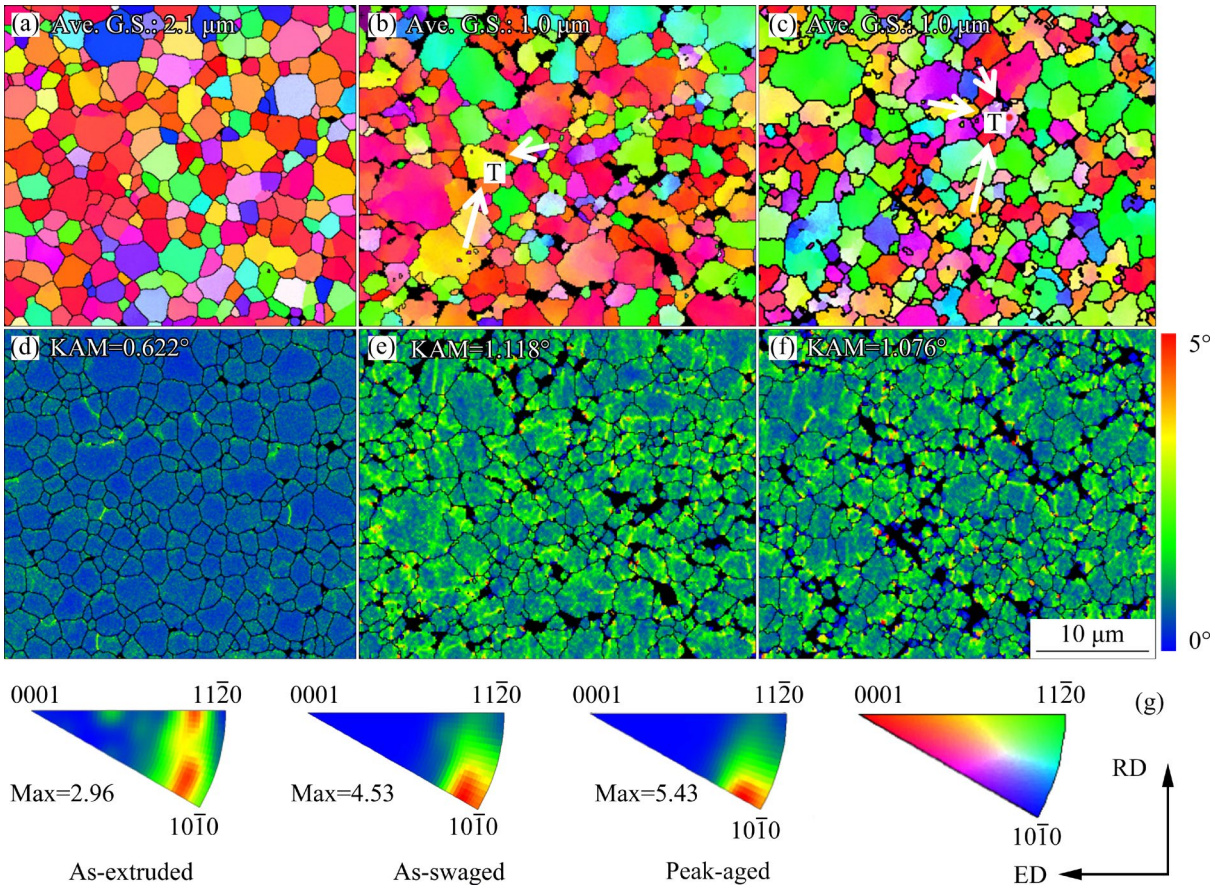

Fig. 1 IPF orientation maps (a−c) and KAM distribution maps (d−f) of as-extruded (a, d), as-swaged (b, e), and peak-aged (c, f) alloys with respect to ED, and corresponding inverse pole figures along RD (g)

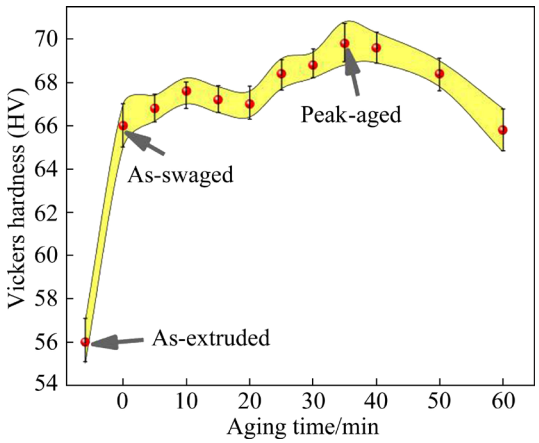

Fig. 2 Vickers hardness distribution of as-extruded, as-swaged, and peak-aged alloys treated at 448 K for different time

formation of geometrically necessary dislocations (GNDs) post-RS treatment. The average KAM values slightly decreased to ~1.076° after aging heat treatment, indicating that only minimal GNDs could be eliminated during short aging durations. Due to the low temperature and short aging time, only a small number of residual dislocations introduced by RS deformation were eliminated.

To further elucidate the mechanisms underlying dislocation activation during the swaging and aging processes, Fig. 3 displays TEM images of the alloys in both the as-swaged and peak-aged conditions, acquired under two-beam diffraction conditions (g=0002 and g=0$\bar{1}$10). Some short dislocation lines were discernible in the as-swaged alloy under g= 0$\bar{1}$10 , which were identified as the ⟨a⟩-component type dislocation. These encompass both basal ⟨a⟩ and non-basal ⟨a⟩ dislocations (marked by brown and yellow arrows in Fig. 3(a), respectively), and this identification was based on the g· b≠0 law. On the other hand, the pyramidal ⟨c⟩ and ⟨c+a⟩ dislocations were detected under g=0002, denoted by blue and red arrows in Fig. 3(b), respectively. As affirmed by MENG et al [32], the intrinsic stacking fault energy is reduced via Ca addition in Mg−Bi−Ca ternary alloy, which can promote the transformation from basal slip to non-basal slip mode.

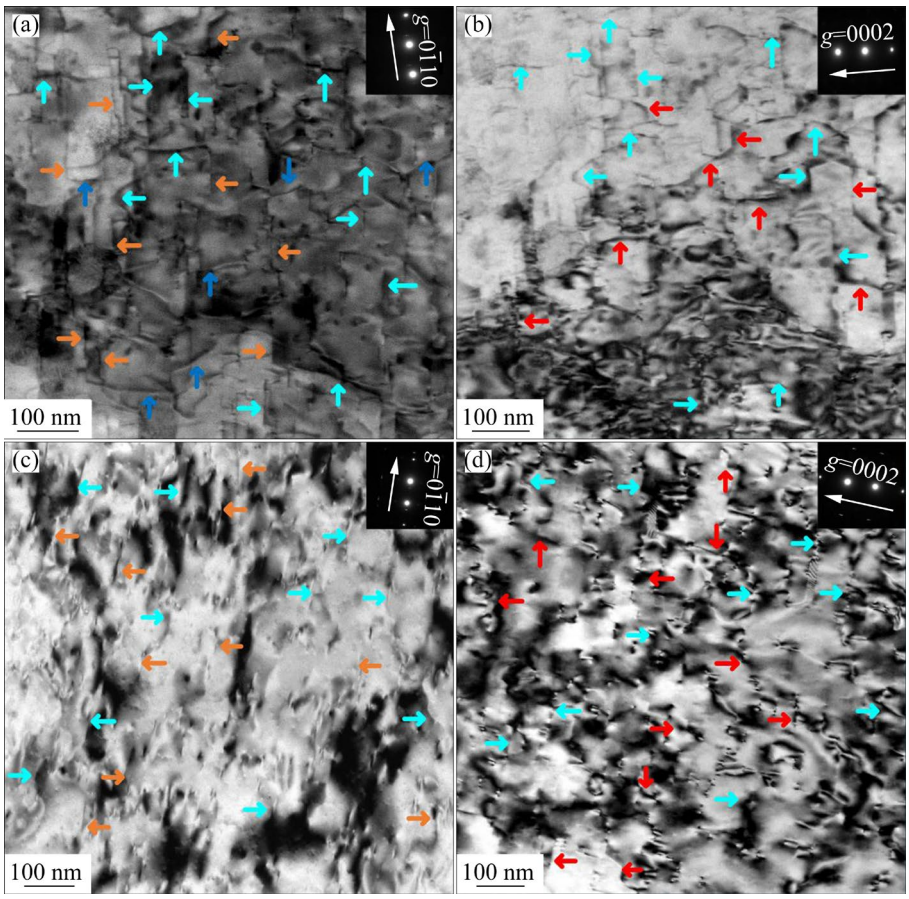

Fig. 3 TEM images of as-swaged (a, b) and peak-aged (c, d) alloys under two-beam diffraction conditions of g=0$\bar{1}$10 (a, c) and g=0002 (b, d), respectively

The dislocation density scarcely decreased in the peak-aged alloy. Similarly, basal ⟨a⟩ and non-basal ⟨a⟩ dislocations were identified under g= 0$\bar{1}$10 , and the pyramidal ⟨c⟩ and ⟨c+a⟩ dislocations were detected under g=0002 based on the $g\cdot b\neq 0$ criterion (Figs. 3(c, d)). The number of basal ⟨a⟩ and non-basal ⟨a⟩ dislocations obviously declined; however, the pyramidal ⟨c⟩ dislocations slightly increased with aging. This can be ascribed to the inherent instability of pyramidal incomplete ⟨c+a⟩ dislocations, which are prone to decomposing into pyramidal ⟨a⟩ and pyramidal ⟨c⟩ dislocations, as discussed in the literature [33]. It is speculated that the ⟨c⟩-component type dislocation increases as the ⟨c+a⟩ dislocations are resolved.

Figure 4 shows the TEM observation of the as-extruded alloy. In conjunction with our previous study [34], both Mg_2Ca and Mg_2Bi_2Ca phases were identified in the BX31 alloy. The crystal structure of the Ca-rich phase was further analyzed using selected area electron diffraction (SAED). The SAED pattern (Fig. 4(a)) and mapping/line scanning (Figs. 4(b−e)) collectively confirm the presence of a uniformly distributed Mg_2Ca phase throughout the matrix, with an average size of approximately 100 nm. Utilizing a similar analytical method, the Mg_2Bi_2Ca phase was detected (Figs. 4(f−j)). In comparison with the Mg_2Ca phase, the Mg_2Bi_2Ca phase exhibits a large size of ~2 μm and is observed to be distributed in banded patterns within the extruded alloy matrix, aligning with macroscopic extrusion flow and parallel to ED. In particular, microcracks were observed in the coarse phases, indicating that the Mg_2Bi_2Ca phase is hard and brittle.

Figure 5 displays the TEM observation of the as-swaged alloy. The Mg_2Ca phase remains present in the matrix, exhibiting no significant changes in its size or number fraction (Figs. 5(a−e)). Nevertheless, compared with the as-extruded alloy, the coarse Mg_2Bi_2Ca phases disappeared after RS. Instead, some finer new phases (~10 nm, Fig. 5(f)) were observed. Based on the SAED and mapping results (Figs. 5(g−j)), these nano-phases were

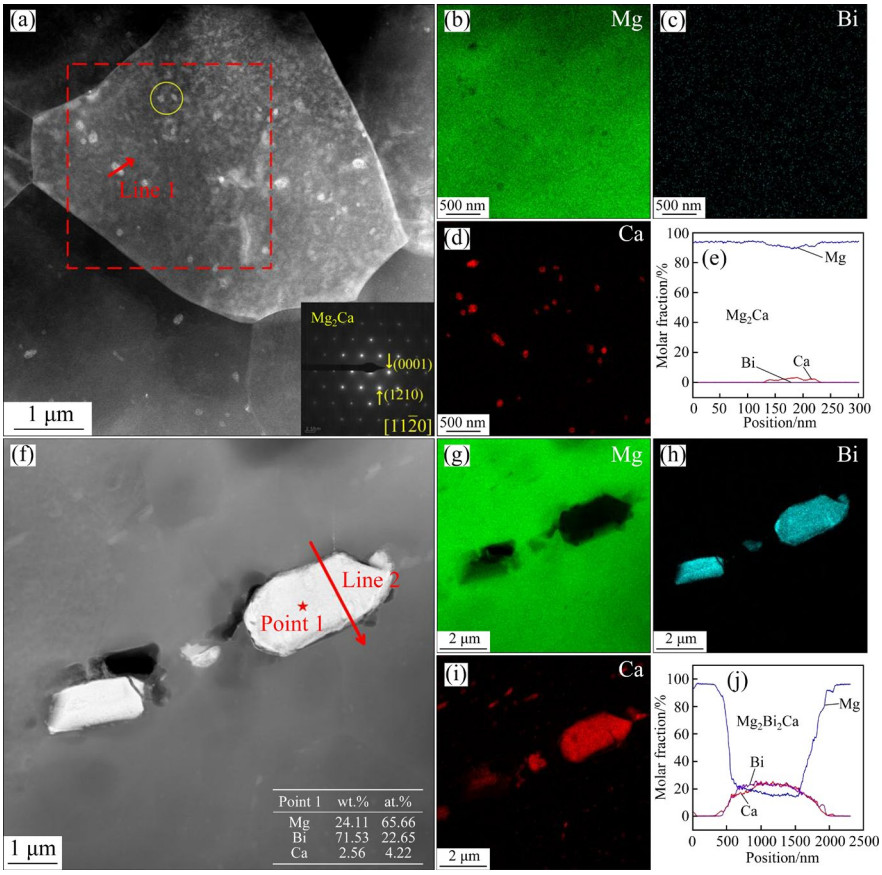

Fig. 4 TEM images and EDS results of Mg_2Ca (a−e) and Mg_2Bi_2Ca (f−j) phases for as-extruded alloy

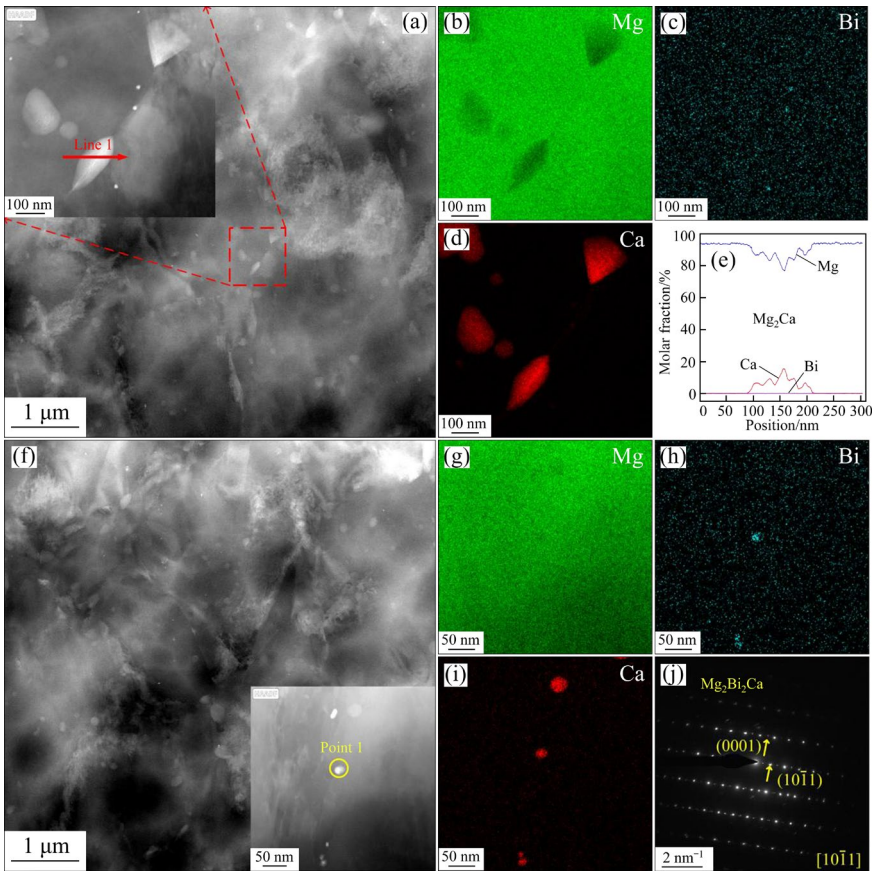

Fig. 5 TEM images and EDS results of Mg_2Ca (a−e) and Mg_2Bi_2Ca (f−j) phases for as-swaged alloy

identified as Mg_2Bi_2Ca, suggesting that the coarse Mg_2Bi_2Ca phases may have been severely fractured during the RS process. Furthermore, the Mg_2Bi_2Ca phases were dispersed throughout the Mg matrix.

Figure 6 shows the TEM results for the peak-aged alloy. Compared with the as-swaged alloy, the sizes of both Mg_2Ca and Mg_2Bi_2Ca phases remained unchanged in the peak-aged alloy. However, the number fraction of both phases rapidly increased from 2.6% to 4.0%, with the Mg_2Bi_2Ca nanophases increasing from 0.5% to 0.9%. A large number of residual dislocations served as precipitation sites for the nano-phase after RS process, which enabled the alloy to reach the peak aging rapidly. The movement of dislocations was impeded differently by the shape, size and location of the precipitates, and the mechanical properties of the matrix were altered [35]. In this work, the shape of the precipitates has been simplified as spherical to facilitate quantification of their contribution to the mechanical property contribution. In addition, it was observed that a limited amount of Ca element had accumulated along the grain boundary of the alloy during the peak aging process (Fig. 6(i)).

Figure 7(a) illustrates the stacking fault in BX31 alloy after RS. WAN et al [28] indicated extensive stacking faults (SFs) on the basal plane and/or dislocation arrays that cut the ultrafine-grained bands into nano-grains. However, the number density of stacking faults is very small in the as-swaged alloy. Therefore, stacking faults are not the main factor in refining grains during RS process.

Dislocation accumulation was observed in the vicinity of the original grain boundaries, as shown in Fig. 7(b). Short non-basal $\langle a \rangle$ dislocations rearrangement distribution occurs inside the grains, as illustrated in Fig. 7(c). Extensive dislocation accumulation and interactions among dislocation arrays led to increased misorientation in the matrix, resulting in the formation of low-angle grain boundaries (LAGBs). WAN et al [28] reported similar dislocation cells in the swaged Mg−Gd−Y−Zr alloy, which were identified as precursors to DRX formation. These LAGBs accumulate through dislocation movement, giving rise to new grains on

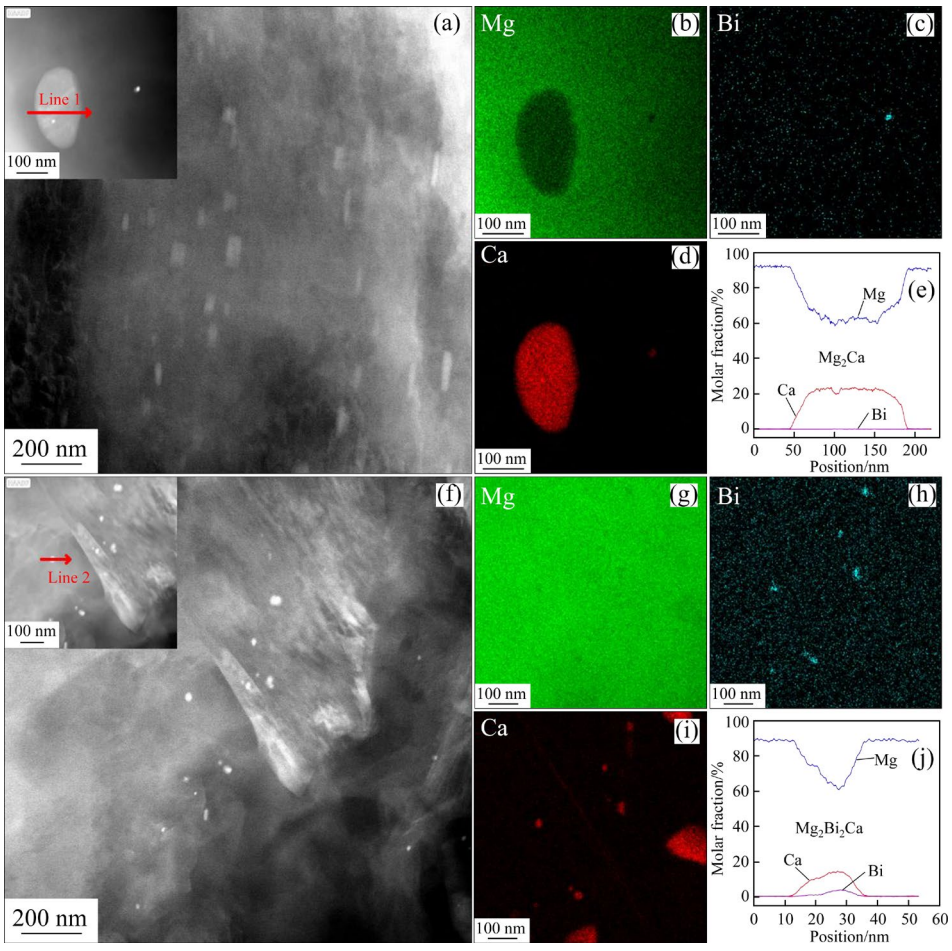

Fig. 6 TEM images and EDS results of Mg_2Ca (a−e) and Mg_2Bi_2Ca (f−j) phases for peak-aged alloy

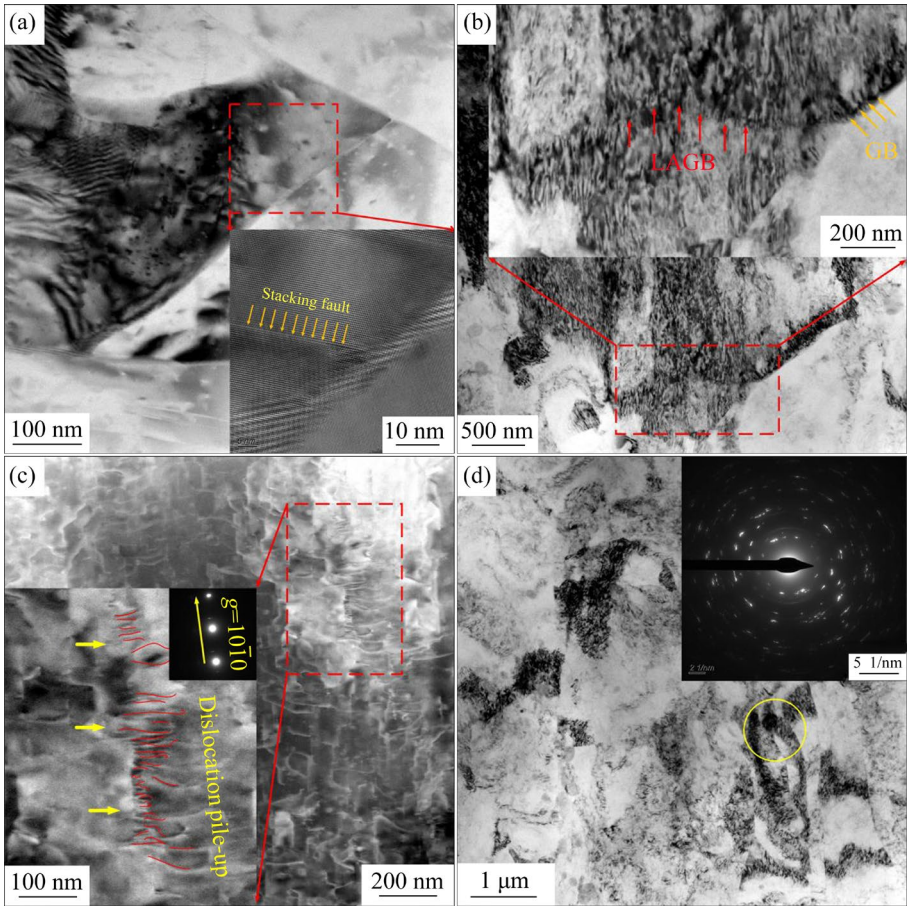

Fig. 7 TEM analysis during RS: (a) Stacking fault; (b) LAGBs near grain boundary; (c) Dislocation arrangement inside grain; (d) Recrystallized structure

existing ones, a process known as continuous dynamic recrystallization (CDRX) [36], leading to grain refinement. This is shown by the ring-like diffraction pattern presented in Fig. 7(d).

3.2 Mechanical properties

Figure 8 shows the tensile true stress−strain curves and corresponding mechanical properties of as-extruded, as-swaged, and peak-aged alloys.

The as-extruded alloy demonstrates a TYS, UTS and elongation to failure (EL) of approximately 193.6 MPa, 347.3 MPa and 16.5%, respectively. Notably, after RS, the TYS and UTS significantly increased to ~318.3 and ~350.0 MPa, respectively. Subsequent peak-aging treatment further enhanced the TYS and UTS to ~358.1 and ~375.8 MPa, respectively. However, the EL decreased from 16.5% to 3.4% and 2.1% after the RS and subsequent aging process, respectively. The strengthening effects of RS and subsequent aging on the as-extruded BX31 alloy are substantial, primarily attributed to grain boundary strengthening,

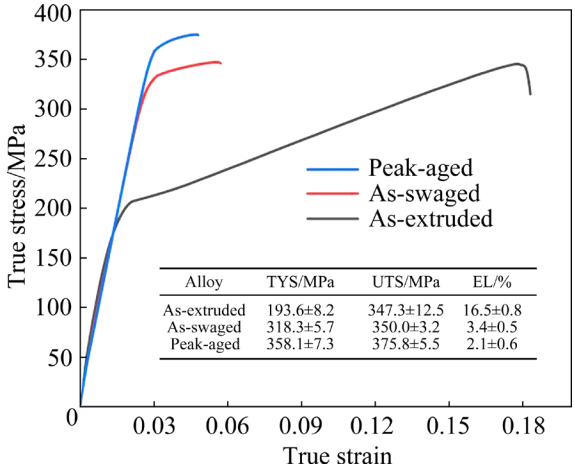

Fig. 8 Tensile true stress−strain curves and corresponding mechanical properties of as-extruded, as-swaged, and peak-aged alloys

dislocation strengthening and precipitation strengthening mechanisms.

To further elucidate the variation in ductility after RS at room temperature, Fig. 9 shows the fracture surfaces and EDS mapping of BX31 alloys

after undergoing tensile testing until failure at RT. Dimples were observed on the surface of as-extruded alloys (Fig. 9(a)), while an extensive cleavage plane was evident on the as-swaged alloy surface (Fig. 9(b)). Similar fracture morphology was also noted in the peak-aged BX31 sample, as shown in Fig. 9(c). The matrix of the as-extruded alloy contained numerous microcracks, whereas microcracks were found to be associated with fragmented second phases after RS and aging processes. Fracture occurred within the Mg_2Bi_2Ca and Mg_2Ca phases of the as-swaged and peak-aged BX31 samples, respectively, as revealed by SEM and EDS mapping analysis. This indicates that fragmented phases may have a detrimental effect on the ductility of the alloy [37]. The brittle phases serve as sources of cracks or fracture origins during tensile deformation, indicated by the cyan arrows, resulting in a significantly reduced tensile EL of the BX31 alloy. A similar influence on ductility for the same reason has also been reported for BX311 alloy by MENG et al [32].

4 Discussion

4.1 Formation mechanisms of fine grains

Figure 10 depicts a schematic diagram of the DRX process of the BX31 alloy during RS and subsequent aging. Dislocations accumulate near the grain boundaries and secondary phases during the

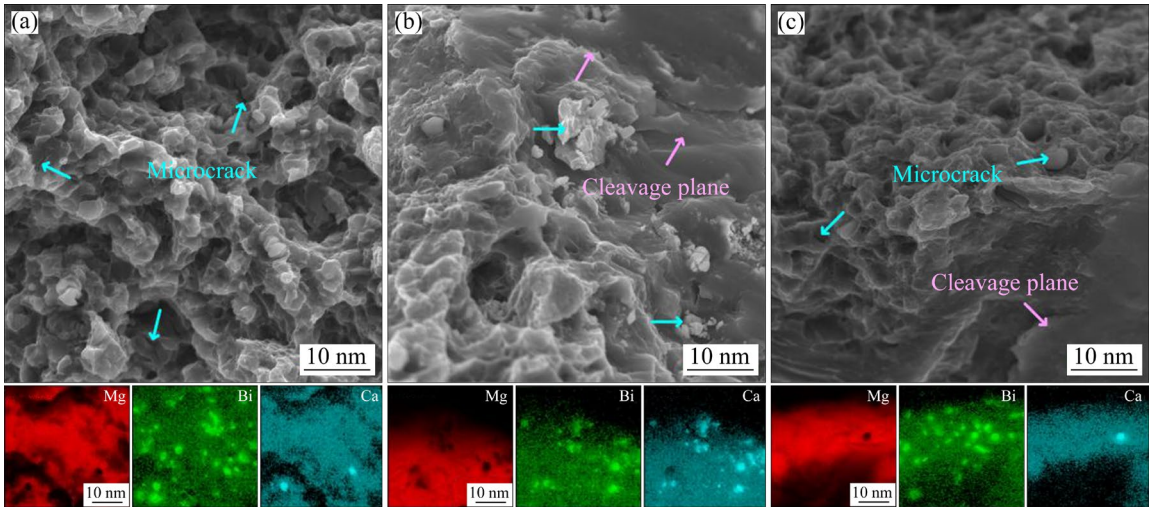

Fig. 9 SEM images of fracture surfaces and corresponding element mapping of BX31 alloys: (a) As-extruded; (b) As-swaged; (c) Peak-aged

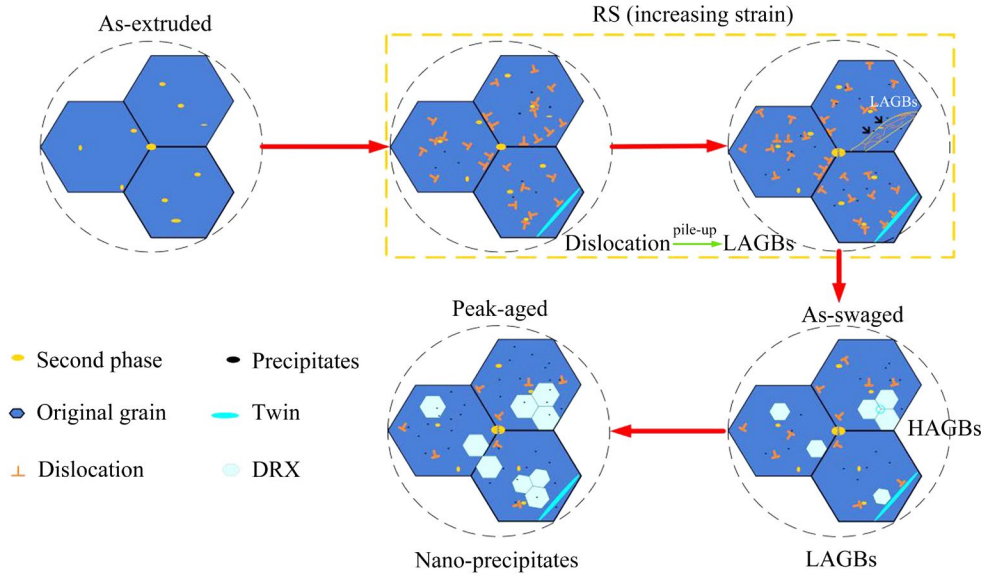

Fig. 10 Schematic diagram of grain refinement of BX31 alloy during RS and subsequent aging

early stages of the RS process. The dislocation density increases as the number of RS passes increases. Dislocation accumulation gives rise to LAGBs with the original grain boundaries as the precursors. The fractured second phases further promote the formation of LAGBs by pinning dislocations. With the continuous progression of the RS process, LAGBs gradually transform into high-angle grain boundaries (HAGBs) due to dislocation pile up, ultimately resulting in the formation of DRX grains. The size of DRX grains gradually enlarges, and local dislocation concentration is alleviated during aging. Due to the decrease in the solid solubility of solute atoms during the RS and aging processes, many nano-phases precipitate, accompanied by Ca segregation near the grain boundary (see Fig. 5(d)).

Compared with BX31 alloy, AZ31 alloy exhibited a higher number of twins, dividing the original coarse grains into fine lamellar twins, resulting in further refinement of the matrix by forming dislocation arrays [26,38,39]. However, only a few twins were observed in this work. It is evident that the dislocation slip plays a crucial role in refining the initial grains of the BX31 alloy during the RS and aging processes.

4.2 Contributions of different strengthening mechanisms

4.2.1 Grain refinement strengthening contribution

From the EBSD results (inset in Fig. 1), it was found that the average grain size of the as-extruded BX31 alloy was 2.1 μm. After RS, the corresponding grain size decreased to 1.0 μm. It is worth noting that the grain size of the as-swaged BX31 alloy remains almost unchanged after aging. The equation used to calculate grain boundary (GB) strengthening σ_d based on the Hall−Petch (H−P) relationship is as follows:

$$\sigma_d=\sigma_0+K\,d^{-1/2} \tag{1}$$

where σ_0 is the yield stress of a single crystal or can be considered as the yield stress of a very coarse-grained polycrystal (about 25 MPa, as tested for cast BX31 alloy, see Fig. S1 in supplementary materials (SM)) [40,41], d is the mean grain diameter, and K is a constant. Previous studies showed that the H−P relation slope (K value) for Mg alloys is dependent on grain size and texture [42]. For as-extruded BX31 alloy, the texture effect is considered to be the same as Ref. [32], and the K value of 173 MPa·μm$^{-1/2}$ [43] was used for the Mg−Bi−Ca alloy. However, the K value changes to approximately 150 MPa·μm$^{-1/2}$ [13,42] when the grain diameter decreases to 1.0 μm. The previously reported value of K for Mg−1.876Zn−0.112Ca (wt.%) alloys was 217 MPa·μm$^{-1/2}$ [10], while the maximum pole density deflection from TD to ED by 15°−20° in the pole figure (and the max pole density nearby $\langle 10\bar{1}0\rangle$ direction in inverse pole figures, as shown in Fig. 1(g)) indicated a texture distribution similar to that of BX31 alloy. Considering both grain size and texture, we selected the middle value of 184 MPa·μm$^{-1/2}$ as the H−P slope after RS and subsequent aging process. The TYS values resulting from grain refinement were calculated for the as-extruded, as-swaged, and peak-aged alloy. The values obtained were 144.4, 209 and 209 MPa, respectively. The TYS variation for both the as-swaged and peak-aged alloys, compared to the as-extruded alloy, was 64.6 MPa.

4.2.2 Dislocation strengthening contribution

The grain store dislocations to accommodate the deformation of the BX31 alloy during the swaging process. High-density residual dislocation tangles generated during the RS process also contribute to the strength of as-swaged alloys. The improvement in yielding strength caused by work hardening can be estimated using the Taylor formula [28,44,45]:

$$\sigma_\rho=M\alpha Gb\rho^{1/2} \tag{2}$$

where the strength increase caused by residual dislocations is denoted by σ_ρ, M is the Taylor factor with a value of 2.1 [28], α is a constant taken as 0.24 [46], G is the shear modulus of Mg equal to 1.66×10^4 MPa, b is the magnitude of the Burgers' vector taken as 0.3202 nm, and ρ is the dislocation density obtained from the XRD (see Fig. S2 in SM) analysis of the peak broadening. The calculation formula is as follows:

$$\rho=1/D^2 \tag{3}$$

where D is the crystal size. It can be calculated by the Scherer equation, and the formula is as follows:

$$D=\frac{k\lambda}{\beta\cos\theta} \tag{4}$$

where k is the Scherer's constant and has a value of 0.89 [47], λ is the X-ray wavelength, equal to

0.154056 nm, and β is the Full width at half maximum (FWHM) corresponding to the position of peak 2θ [48].

The final calculated dislocation strengthening values are shown in Table 1.

Table 1 Dislocation strengthening contribution at different states

State	ρ/nm^{-2}	σ_ρ/MPa	$\Delta\sigma_\rho$/MPa
As-extruded	0.000063	21.2	–
As-swaged	0.000846	77.9	56.7
Peak-aged	0.000705	71.1	49.9

It can be seen from the results in Table 1 that the dislocation strengthening effect during RS process is slightly lower, at about 56.7 MPa, compared to the GB strengthening contribution of 64.6 MPa. The dislocation density of the as-swaged BX31 alloy slightly decreased after the aging process, producing a slightly lower strength of approximately 49.9MPa.

4.2.3 Precipitation strengthening contribution

The size of the second phase is refined to the nano-scale by radial stress during RS. During aging, some nano-phases continuously precipitate, impeding the movement of dislocations. The strengthening contribution of nano-phases can be calculated according to the formula of the mechanism in Orowan [35,49,50]:

$$\sigma_{\mathrm{P}}=\frac{MGb}{2\pi\sqrt{1-\nu}\left(\frac{0.779}{\sqrt{f_{\mathrm{p}}}}-0.785\right)d_{\mathrm{p}}}\ln\frac{0.785d_{\mathrm{p}}}{\vec{b}} \quad (5)$$

The Poisson ratio (υ) is taken as ~0.3. Here, d_{p} and f_{p} represent the mean radius and volume fraction of the precipitated phase, respectively.

TEM was used to calculate the average size and volume fraction of the second phase in the three states. The statistical results are shown in Table 2. Showing that the volume fraction of the precipitates increased from ~1.8% in the as-extruded state to ~2.6% in the as-swaged state and then to ~4.0% in the peak-aged alloy.

It can be calculated that the precipitation strengthening values for as-extruded, as-swaged, and peak-aged are 43.3, 51.7 and 87.4 MPa, respectively. The contributions of the main strengthening mechanisms are listed in Table 3.

Table 2 Statistical results of average size and volume fraction of precipitated phase at different states

State	Phase size/nm	Average size/nm	Volume fraction/%
As-extruded	>25	56.0	1.7
	<25	9.6	0.1
As-swaged	>25	52.0	2.1
	<25	9.6	0.5
Peak-aged	>25	51.0	3.1
	<25	7.1	0.9

Table 3 Contribution of strengthening mechanisms on TYS of BX31 alloy at different states

State	σ_{d}/MPa	σ_ρ/MPa	σ_{P}/MPa
As-extruded	144.4	21.2	43.3
As-swaged	209.0	77.9	51.7
Peak-aged	209.0	71.1	87.4

The strengthening effect of the BX31 alloy after RS deformation is mainly provided by the GB strengthening (64.6 MPa) and dislocation strengthening (56.7 MPa), and the precipitation strengthening contribution is weakened (8.4 MPa). The alloy strength can be further enhanced through peak-aging after RS deformation. The strengthening contributions are mainly refinement strengthening (64.6 MPa, the calculated grain size did not change in the as-swaged BX31 alloy, therefore, the effect of refinement strengthening is the same as that after RS), dislocation strengthening (49.9 MPa, a small amount of dislocation accumulation introduced by RS can be eliminated after aging treatment, thus the strengthening effect is weaker than that in the as-swaged state), and precipitation strengthening (44.1 MPa). The TYS was calculated using an empirical equation, resulting in values that are similar to those obtained from tensile tests.

Furthermore, the typical basal fiber texture was observed after RS. Accordingly, the SF value for basal slip is low, which is 0.216 when tension occurred along with the RS direction. According to the literature [51], the relationship between the yield strength and the SF for basal slip has been proposed. It can be seen that the strength increases with the decrease of SF value.

ZHAI et al [49] reported that Ca segregation can occur in Mg alloys at RT, and that a minor solid solution strengthening effect is caused by Ca atoms.

However, the Ca content is low in the BX31 alloy, thus, its contribution to strengthening is not considered here. On the other hand, the SFs may significantly influence dislocation movement and cross-slip during the plastic deformation process, thereby affecting mechanical properties considerably [52,53]. Previous research [29,54] has suggested that there is a linear relationship between yield strength and the reciprocal of the average SFs spacing in Mg alloys. Similarly, given that only a limited number of SFs were observed in the as-swaged alloy, their impact on strength can be deemed negligible.

4.3 Ductility change of BX31 alloy after swaging and subsequently aging

Currently, the paradox of balancing ductility and strength remains unresolved for metals that have undergone cold deformation. In the case of Mg alloys, the yield strength increases while ductility decreases during RS deformation. Swaging reduces grain size, thereby enhancing the strength of the BX31 alloy. However, a finer grain structure may accommodate fewer dislocations due to an increased number of GBs. During tensile testing, the activity of dislocations is impeded by GBs, resulting in a concentration of dislocations near the GBs. Additionally, substantial residual dislocations were retained in the α-Mg matrix after RS and the subsequent aging process, as depicted in the KAM maps of Figs. 1(d−f). The dislocation storage capacity of fine grains decreases due to the high density of residual dislocations. The presence of residual dislocations promotes the emergence of micro-stress concentrations, which significantly contribute to reduced ductility during tensile testing. The ductility decreased from 16.5% to 3.4% and 2.1% for the as-swaged and peak-aged BX31 alloys, respectively.

In addition, the relationship between the ductility and the SF for basal slip is presented in the literature [51]. That equation shows that the SF value for basal $\langle a \rangle$ slip is proportional to the ductility of the Mg alloy. For BX31 alloy, the ductility decreases with a decrease of SF after RS and the subsequent aging process. The ductility of the BX31 alloys was drastically reduced due to residual dislocations and texture.

5 Conclusions

(1) This work presents a Mg−3.2Bi−0.8Ca ternary alloy with a high yield strength of ~358.1 MPa fabricated by hot extrusion, room temperature RS and subsequent aging treatment. The yield strength exceeds that of most non-RE Mg alloys.

(2) After peak-aging, a certain amount of nanoscale Mg_2Bi_2Ca phases continuously precipitated. The high strength of the peak-aged alloy was mainly attributed to grain boundary strengthening (~209 MPa), dislocation strengthening (~71 MPa), and precipitation strengthening (~87 MPa). However, the ductility of BX31 alloys decreased with increasing strain hardening.

(3) Grain refinement was achieved in the as-extruded BX31 alloy using the RS technique, mainly through the CDRX mechanism. Based on the original grain boundaries, LAGBs were formed through dislocation accumulation. The LAGBs gradually transformed into HAGBs as strain increased, and finally evolved into DRX grains, thereby refining the grain structure.

CRediT authorship contribution statement

Yang CHEN: Investigation, Experimental analysis, Writing − Original draft, Writing − Review & editing; **Jun-jie HE:** Investigation, Writing − Review & editing, Project administration, Funding acquisition; **Kun YANG:** Investigation, Experimental analysis; **Qiu-yan HUANG:** Investigation, Funding acquisition; **Hui-jun HAO:** Investigation; **Yi-lun ZHOU:** Investigation; **Wei-qi WANG:** Investigation; **Kai XIONG:** Writing − Review & editing; **Yong MAO:** Project administration, Funding acquisition; **Qing-hang WANG:** Writing − Review & editing, Project administration, Funding acquisition.

Declaration of competing interest

The authors declare that they have no known competing financial interests or personal relationships that could have appeared to influence the work reported in this paper.

Acknowledgments

This work was supported by the financial supports from the National Key Research and Development Program of China (No. 2021YFB3701100), the National Natural Science Foundation of China (Nos. 51901204, 52161023, 52204407), Key Research and Development

Plan of Shanxi Province, China (No. 202102050201005), Science and Technology Project of Yunnan Precious Metal Laboratory, China (No. YPML-2023050208), Yunnan Science and Technology Planning Project, China (Nos. 202201AU070010, 202301AT070276, 202302AB080008, 202303AA080001), and the Second Professional Practice Innovation Project of Yunnan University, China (No. ZC-22221620).

Supplementary Materials

Supplementary Materials in this paper can be found at: https://tnmsc.csu.edu.cn/download/06-p4050-2024-0543-Supplementary_Materials.pdf.

References

[1] LIU Lei, ZHOU Xiao-jie, YU Shi-lun, ZHANG Jian, LU Xian-zheng, SHU Xin, SU Zai-jun. Effects of heat treatment on mechanical properties of an extruded Mg−4.3Gd−3.2Y−1.2Zn−0.5Zr alloy and establishment of its Hall−Petch relation [J]. Journal of Magnesium and Alloys, 2022, 10(2): 501−512.

[2] SHI Hai-long, XU Chao, HU Xiao-shi, GAN Wei-min, WU Kun, WANG Xiao-jun. Improving the Young's modulus of Mg via alloying and compositing — A short review [J]. Journal of Magnesium and Alloys, 2022, 10(8): 2009−2024.

[3] MENG Shuai-ju, YU Hui, FAN Shao-da, LI Qi-zhi, PARK S H, SUH J S, KIM Y M, NAN Xiao-long, BIAN Ming-zhe, YIN Fu-xing, ZHAO Wei-min, YOU B S, SHIN K S. Recent progress and development in extrusion of rare earth free Mg alloys: A review [J]. Acta Metallurgica Sinica (English Letters), 2019, 32(2): 145−168.

[4] NAKATA T, XU C, KAIBE K, YOSHIDA Y, YOSHIDA K, KAMADO S. Improvement of strength and ductility synergy in a room-temperature stretch-formable Mg−Al−Mn alloy sheet by twin-roll casting and low-temperature annealing [J]. Journal of Magnesium and Alloys, 2022, 10(4): 1066−1074.

[5] WU Fan, WANG Meng, DU Zhi-wen, SHI Ruo-lan, SHANG Qi, LIU Ting-ting, GUO Ning, GUO Sheng-feng, SONG Bo. Influence of free-end torsion on compressive behavior of extruded AZ31 rod at various temperatures [J]. Transactions of Nonferrous Metals Society of China, 2022, 32(11): 3563−3577.

[6] LI J R, XIE D S, ZENG Z R, SONG B, XIE H B, PEI R S, PAN H C, REN Y P, QIN G W. Mechanistic investigation on Ce addition in tuning recrystallization behavior and mechanical property of Mg alloy [J]. Journal of Materials Science & Technology, 2023, 132: 1−17.

[7] JIANG M G, XU C, NAKATA T, YAN H, CHEN R S, KAMADO S. Rare earth texture and improved ductility in a Mg−Zn−Gd alloy after high-speed extrusion [J]. Materials Science and Engineering: A, 2016, 667: 233−239.

[8] SHANG Qi, WU Fan, CHEN Hong-bing, ZHANG Hong-ju, LIU Ting-ting, GUO Ning, GUO Sheng-feng, SONG Bo. Enhancing tensile properties of extruded AZ31 rod by introducing gradient bimodal microstructure [J]. Transactions of Nonferrous Metals Society of China, 2023, 33(12): 3673−3684.

[9] PAN Hu-cheng, QIN Gao-wu, HUANG Yun-miao, REN Yu-ping, SHA Xue-chao, HAN Xiao-dong, LIU Zhi-Quan, LI Caifu, WU Xiao-lei, CHEN Hou-wen, HE Cong, CHAI Lin-jiang, WANG Yun-zhi, NIE Jian-feng. Development of low-alloyed and rare-earth-free magnesium alloys having ultra-high strength [J]. Acta Materialia, 2018, 149: 350−363.

[10] DU Yu-zhou, DU Wei, ZHANG Dan-li, GE Yan-feng, JIANG Bai-ling. Enhancing mechanical properties of an Mg−Zn−Ca alloy via extrusion [J]. Materials Science and Technology, 2021, 37(6): 624−631.

[11] PAN Hu-cheng, KANG Rui, LI Jing-ren, XIE Hong-bo, ZENG Zhuo-ran, HUANG Qiu-yan, YANG Chang-lin, REN Yu-ping, QIN Gao-wu. Mechanistic investigation of a low-alloy Mg−Ca-based extrusion alloy with high strength–ductility synergy [J]. Acta Materialia, 2020, 186: 278−290.

[12] JIN S C, LEE J U, GO Jong-bin, YU Hui, PARK S H. Effects of Sn addition on the microstructure and mechanical properties of extruded Mg−Bi binary alloy [J]. Journal of Magnesium and Alloys, 2022, 10(3): 850−861.

[13] LUO Yi-hao, CHENG Wei-li, LI Hang, YU Hui, WANG Hong-xia, NIU Xiao-feng, WANG Li-fei, YOU Zhi-yong, HOU Hua. Achieving high strength-ductility synergy in a novel Mg−Bi−Sn−Mn alloy with bimodal microstructure by hot extrusion [J]. Materials Science and Engineering: A, 2022, 834: 142623.

[14] REMENNIK S, BARTSCH I, WILLBOLD E, WITTE F, SHECHTMAN D. New, fast corroding high ductility Mg−Bi−Ca and Mg−Bi−Si alloys, with no clinically observable gas formation in bone implants [J]. Materials Science and Engineering: B, 2011, 176(20): 1653−1659.

[15] MENG Shuai-ju, ZHANG Ming-chi, XIAO Hao-ran, LUO Zhan-ju, YU Wei, JIANG Run-lin, CHENG Xue-qi, WANG Li-dong. A superior high-strength dilute Mg−Bi−Ca extrusion alloy with a bimodal microstructure [J]. Metals, 2022, 12(7): 1162.

[16] MENG S J, YU H, FAN S D, KIM Y M, PARK S H, ZHAO W M, YOU B S, SHIN K S. A high-ductility extruded Mg−Bi−Ca alloy [J]. Materials Letters, 2020, 261: 127066.

[17] CHEN Yang, WANG Qing-hang, WANG Li, ZHAI Hao-wei, HUANG Li-xin, JIANG Bin, MAO Yong, HE Jun-jie. Deformation mechanisms of as-extruded Mg−3Bi−1Ca (wt.%) alloy during room-temperature tension [J]. Materials Science and Engineering: A, 2023, 875: 145119.

[18] ESTRIN Y, VINOGRADOV A. Extreme grain refinement by severe plastic deformation: A wealth of challenging science [J]. Acta Materialia, 2013, 61(3): 782−817.

[19] ZHANG Zhi, ZHANG Jing-huai, WANG Jun, LI Ze-hua, XIE Jin-shu, LIU Shu-juan, GUAN Kai, WU Rui-zhi. Toward the development of Mg alloys with simultaneously improved strength and ductility by refining grain size via the deformation process [J]. International Journal of Minerals Metallurgy and Materials, 2021, 28(1): 30−45.

[20] LI Yan-sheng, WANG Jin-hui, XU Rui. The microstructure and mechanical properties of nanocrystalline Mg−Zn−Y alloy achieved by a combination of aging and high pressure torsion [J]. Vacuum, 2020, 178: 109396.

[21] JIANG Ju-fu, LIN Xin, WANG Ying, QU Jian-jun, LUO Shou-jing. Microstructural evolution of AZ61 magnesium alloy predeformed by ECAE during semisolid isothermal treatment [J]. Transactions of Nonferrous Metals Society of China, 2012, 22(3): 555−563.

[22] LANGDON T G. Twenty-five years of ultrafine-grained materials: Achieving exceptional properties through grain refinement [J]. Acta Materialia, 2013, 61(19): 7035−7059.

[23] ZHANG Nian-xian, KAWASAKI M, DING Hua, LANGDON T G. An examination of microstructural evolution and homogeneity in a magnesium AZ80 alloy processed by high-pressure torsion [J]. Materials Science and Engineering: A, 2021, 806: 140832.

[24] MODINA I M, POLYAKOV A V, DYAKONOV G S, YAKOVLEVA T V, RAAB A G, SEMENOVA I P. Peculiarities of microstructure and mechanical behavior of VT8M-1 alloy processed by rotary swaging [J]. IOP Conference Series: Materials Science and Engineering, 2018, 461: 012056.

[25] CHEN J K, CHEN Y C, LI H T, CHAN K S, CHANG C J. Effects of Nd and rotary forging on mechanical properties of AZ71 Mg alloys [J]. Transactions of Nonferrous Metals Society of China, 2015, 25(10): 3223−3231.

[26] CHEN Xin, LIU Chu-ming, JIANG Shu-nong, CHEN Zhi-yong, WAN Ying-chun. Effect of yttrium on nanocrystallization of magnesium alloys during cold rotary swaging [J]. Materials Characterization, 2022, 184: 111696.

[27] CHEN Xin, LIU Chu-ming, FANG Meng, JIANG Shu-nong, CHEN Zhi-yong, WAN Ying-chun. Strengthening the Mg−Y−Zn alloy through the formation of nanoscale lamellar structures and nanograins [J]. Journal of Alloys and Compounds, 2021, 886: 161148.

[28] WAN Ying-chun, TANG Bei, GAO Yong-hao, TANG Ling-ling, SHA Gang, ZHANG Bo, LIANG Ning-ning, LIU Chu-ming, JIANG Shu-nong, CHEN Zhi-yong, GUO Xue-yi, ZHAO Yong-hao. Bulk nanocrystalline high-strength magnesium alloys prepared via rotary swaging [J]. Acta Materialia, 2020, 200: 274−286.

[29] HUANG Zhao-yi, LIU Chu-ming, JIANG Shu-nong, XIAO Hong-chao, CHEN Xin, WAN Ying-chun, ZENG Gang. Achieving high-strength nanocrystalline WE43 Mg alloy by a combination of cold rotary swaging and aging treatment [J]. Vacuum, 2022, 197: 110840.

[30] LIU Y H, ZHANG Z R, WANG J, LI Y, LI H X, JIA L Y, WANG J H, ZHANG J S. A novel Mg−Gd−Y−Zn−Cu−Ni alloy with excellent combination of strength and dissolution via peak-aging treatment [J]. Journal of Magnesium and Alloys, 2023, 11(2): 720−734.

[31] KIM W J, JEONG H G, JEONG H T. Achieving high strength and high ductility in magnesium alloys using severe plastic deformation combined with low-temperature aging [J]. Scripta Materialia, 2009, 61(11): 1040−1043.

[32] MENG Shuai-ju, YU Hui, LI Li-chao, QIN Jia-nan, WOO S K, GO Y H, KIM Y M, PARK S H, ZHAO Wei-min, YIN Fu-xing, YOU B S, SHIN K S. Effects of Ca addition on the microstructures and mechanical properties of as-extruded Mg−Bi alloys [J]. Journal of Alloys and Compounds, 2020, 834: 155216.

[33] WU Z X, CURTIN W A. The origins of high hardening and low ductility in magnesium [J]. Nature, 2015, 526(7571): 62−67.

[34] WANG Qing-hang, WANG Li, ZHAI Hao-wei, CHEN Yang, CHEN Shuai. Establishment of constitutive model and analysis of dynamic recrystallization kinetics of Mg−Bi−Ca alloy during hot deformation [J]. Materials, 2022, 15(22): 7986.

[35] NIE J F. Effects of precipitate shape and orientation on dispersion strengthening in magnesium alloys [J]. Scripta Materialia, 2003, 48(8): 1009−1015.

[36] HUANG K., LOGÉ R E. A review of dynamic recrystallization phenomena in metallic materials [J]. Materials & Design, 2016, 111: 548−574.

[37] CHEN Xiang, WANG Wei-zhang, ZHANG Jun-lei, HUANG Guang-sheng, LIU Shuai-shuai, TANG Ai-tao, JIANG Bin, PAN Fu-sheng. Tailoring AZ91 laminates for combination of strength and ductility [J]. Transactions of Nonferrous Metals Society of China, 2021, 31(12): 3703−3718.

[38] CHEN Xin, LI Si-long, WAN Ying-chun. The effect of initial grain size on the nanocrystallization of AZ31 Mg alloy during rotary swaging [J]. Materials, 2022, 15(22): 7979.

[39] FAN Yu-tian, LU Li-wei, LIU Jian-bo, MA Min, HUANG Wei-ying, WU Rui-zhi. Effect of deformation temperature on microstructure and texture of AZ31 magnesium alloy processed by new plastic deformation method [J]. Transactions of Nonferrous Metals Society of China, 2024, 34(7): 2138−2152.

[40] LU Song-jiang, KAN Qian-hua, ZAISER M, LI Zhen-huan, KANG Guo-zheng, ZHANG Xu. Size-dependent yield stress in ultrafine-grained polycrystals: A multiscale discrete dislocation dynamics study [J]. International Journal of Plasticity, 2022, 149: 103183.

[41] TROJANOVÁ Z K, DROZD Z, HALMEŠOVÁ K, DŽUGAN J, ŠKRABAN T, MINÁRIK P, NÉMETH G, LUKÁČ P. Strain hardening in an AZ31 alloy submitted to rotary swaging [J]. Materials, 2020, 14(1): 157.

[42] RAZAVI S M, FOLEY D C, KARAMAN I, HARTWIG K T, DUYGULU O, KECSKES L J, MATHAUDHU S N, HAMMOND V H. Effect of grain size on prismatic slip in Mg−3Al−1Zn alloy [J]. Scripta Materialia, 2012, 67(5): 439−442.

[43] CHEN Lian-yi, XU Jia-quan, CHOI H, POZUELO M, MA Xiao-long, BHOWMICK S, YANG J M, MATHAUDHU S N, LI Xiao-chun. Processing and properties of magnesium containing a dense uniform dispersion of nanoparticles [J]. Nature, 2015, 528(7583): 539−543.

[44] FU Li, GE Hua-long, HE Jun-jie, XIONG Kai, ZHU Li-xian, GAN Xu, LIU Yi, FU Quan, MA Li-hua, LU Shao-ping, MAO Yong. Phase formation, microstructure evolution and strengthening mechanism of $Au_{27.9}Ag_{20.3}Cu_{51.8}$ noble metal medium-entropy alloy during cold deformation and aging [J]. Materials Science and Engineering: A, 2023, 887: 145733.

[45] ZHANG Wei, SHEN Zhi-peng, PAN Hu-cheng, WANG Tao, FU Tong, XIE Dong-sheng, TANG Ai-tao, TENG Chang-qing, WU Lu, QIN Gao-wu. Enhancing strength and irradiation tolerance of Mg alloy via co-addition of Mn and Ca elements [J]. Journal of Materials Science & Technology, 2025, 216: 38−51.

[46] HANSEN N, HUANG X. Microstructure and flow stress of

polycrystals and single crystals [J]. Acta Materialia, 1998, 46(5): 1827−1836.

[47] NSAIF F K, MOHAMMED J S, MOHAMMED I A, JASIM K A. Preparation and study the structural properties for compound $Tl_{0.9}Hg_{0.1}Sr_2Ca_2Cu_3O_{8+\delta}$ using the modified Scherer equation [J]. IOP Conference Series: Materials Science and Engineering, 2022, 1258(1): 012008.

[48] UNGÁR T. Microstructural parameters from X-ray diffraction peak broadening [J]. Scripta Materialia, 2004, 51(8): 777−781.

[49] ZHAI Hao-wei, WANG Li, WANG Qing-hang, LI Meng, CHAI Yan-fu, XU Jun, JIANG Bin. Achieving high strength near 400 MPa in an ultra-fine grained Mg−Bi−Ca ternary alloy via low-temperature extrusion [J]. Journal of Materials Research and Technology, 2023, 26: 3973−3991.

[50] LI Xin-yu, XIA Wei-jun, CHEN Ji-hua, YAN Hong-ge, LI Zhen-zhen, SU Bin, SONG Min. Dynamic recrystallization, texture and mechanical properties of high Mg content Al−Mg alloy deformed by high strain rate rolling [J]. Transactions of Nonferrous Metals Society of China, 2021, 31(10): 2885−2898.

[51] WANG Qing-hang, SHEN Ya-qun, JIANG Bin, TANG Ai-tao, YANG Tian-hao, HUANG Guang-sheng, PAN Fu-sheng. A micro-alloyed Mg−Sn−Y alloy with high ductility at room temperature [J]. Materials Science and Engineering: A, 2018, 735: 131−144.

[52] HE C, ZHANG Y, LIU C Q, YUE Y, CHEN H W, NIE J F. Unexpected partial dislocations within stacking faults in a cold deformed Mg−Bi alloy [J]. Acta Materialia, 2020, 188: 328−343.

[53] JIAN W W, CHENG G M, XU W Z, YUAN H, TSAI M H, WANG Q D, KOCH C C, ZHU Y T, MATHAUDHU S N. Ultrastrong Mg alloy via nano-spaced stacking faults [J]. Materials Research Letters, 2013, 1(2): 61−66.

[54] CHEN Xin, LI Si-long, WAN Ying-chun. Effect of Gd on preparation of nanocrystalline Mg alloys via cold rotary swaging [J]. Transactions of Nonferrous Metals Society of China, 2024, 34(6): 1817−1828.

通过旋锻和时效处理获得高强度的挤压态 Mg−Bi−Ca 三元合金

陈 阳[1]，何俊杰[1]，杨 锟[1]，黄秋艳[2]，郝惠军[1]，周逸伦[1]，王伟奇[1]，熊 凯[1]，毛 勇[1]，王庆航[3]

1. 云南大学 材料与能源学院 材料基因工程研究中心，昆明 650504；
2. 中国科学院 金属研究所，沈阳 110016；
3. 扬州大学 机械工程学院，扬州 225127

摘 要：通过热挤压、室温旋锻及后续时效处理制备了屈服强度为~358.1 MPa 的 Mg−3.2Bi−0.8Ca(BX31，质量分数，%)三元合金。挤压态合金显微组织晶粒细小(~2 μm)，呈现弱的非基面织构且存在少量第二相。在室温旋锻过程中发生连续动态再结晶，使得合金的平均晶粒尺寸减小至~1 μm。另外，在晶粒内部存在大量的残余位错堆积，且在位错附近观察到纳米析出相。合金在 448 K 时效 35 min 后出现硬度峰值，晶粒尺寸几乎未发生变化，而残余位错的密度略有降低，位错堆积区域出现大量纳米析出相。晶界强化、位错强化和析出强化是合金在时效后强度增加的主要因素。

关键词：Mg−Bi−Ca 合金；旋锻变形；时效；连续动态再结晶；析出

(Edited by Xiang-qun LI)